

# Micrometer-scale displacement and thickness sensing using a single terahertz resonant-tunneling diode

---

Li Yi<sup>1,2</sup>, Shota Ito<sup>1</sup>, Chao Tang<sup>3</sup>, Yousuke Nishida<sup>4</sup>, Koji Terumoto<sup>4</sup>, Toshihisa Maeda<sup>4</sup>, Yuta Inose<sup>2</sup>, and Masayuki Fujita<sup>2</sup>

1 Graduate School of Science and Engineering, Ibaraki University, Hitachi, Japan

2 Graduate School of Engineering Science, The University of Osaka, Toyonaka, Japan

3 Frontier Research Institute for Interdisciplinary Sciences, Tohoku University, Sendai, Japan

4 ROHM Research & Development Center, ROHM Co., Ltd., Kyoto, Japan

## Abstract

Resonant tunneling diodes (RTDs) provide room-temperature terahertz oscillation and strong nonlinear mixing, enabling compact monostatic sensors in which a single device acts as both a bias-tunable oscillator and a self-oscillating mixer. This paper presents a 280 GHz-band radar concept enabled by a single RTD, which exploits self-mixing to generate a low-frequency radar interferometric signal while sweeping the RTD oscillation frequency. We show that the RTD self-mixing waveform can be interpreted from a radar perspective and processed to extract micrometer-scale displacement and thin-film thickness changes from repeated sweeps. Using the proposed technique, we experimentally demonstrate a minimum detectable displacement of  $\sim 5 \mu\text{m}$  and quantitatively resolve polymer film thicknesses of 12.5, 25, and 50  $\mu\text{m}$ .

Index Terms—Terahertz sensing, interferometric radar, resonant tunneling diode (RTD), self-mixing.

Contributions:

- 1) Single-device THz transceiver: A single RTD is operated as both a bias-tunable oscillator and a self-oscillating mixer via self-mixing.
- 2) Low-frequency control/readout: The sensing signal is confined to sub-MHz bandwidth, enabling low-cost MHz-rate acquisition electronics.
- 3) Interferometric processing: A phase-based processing approach and a simple phase estimator are introduced for micrometer-order displacement/thickness sensing.

## I. INTRODUCTION

Terahertz (THz) wave ( $\sim 0.1\text{--}10 \text{ THz}$ ) provides a unique combination of sub-millimeter-scale wavelength, material-dependent dielectric response, and the ability to penetrate many common

nonconducting materials. These properties motivate a wide range of nondestructive evaluation, imaging, and metrology applications [1-5]. Among established techniques, terahertz time-domain spectroscopy (THz-TDS) provides broadband permittivity extraction and time-of-flight-based thickness/distance estimation [3-4], but its reliance on femtosecond lasers and complex optoelectronics limits system compactness and cost efficiency.

As an alternative, continuous-wave (CW) radar approaches offer an attractive alternative when compactness and low power are prioritized [2,5-9]. The CW radar technique is commonly implemented using amplitude- or frequency-modulated continuous-wave (AMCW/FMCW) techniques, which translate target distance into a measurable phase delay term [6]. These approaches eliminate ultrafast optical components and enable phase and spectrum processing in THz-band systems, with many successful applications have already been reported [2,5,10-13]. However, they typically rely on high-end THz hardware, including a tunable high-frequency source as well as dedicated transmit, receive, and mixing chains. Although CMOS/SiGe-based solutions have become increasingly practical toward the sub-THz band, efficient implementations above 300 GHz remain challenging in terms of output power, tuning range, and front-end loss [11-12].

To further improve system integration and reduce cost at terahertz frequencies, resonant tunneling diodes (RTDs) have emerged as attractive candidates owing to their ability to sustain room-temperature THz oscillation together with strong intrinsic nonlinearity [13–15]. Numerous sensing applications have demonstrated their remarkable sensitivity and high level of integrability [18-21]. Notably, RTDs can also operate under injection-locking conditions [16,17], a phenomenon extensively studied in laser technology [22-24]. This mechanism has been shown to enhance the sensitivity of THz-band detectors [17] and suggests additional opportunities for sensing applications. Recently, we demonstrated THz-band three-dimensional radar imaging using a single RTD operating in a self-mixing configuration, in which the signal reflected from the target is reinjected into the same RTD [18]. This approach highlights significant advantages in system size, cost, and power consumption compared with conventional THz radar architectures.

In this work, we leverage RTD self-mixing in combination with an interferometric radar technique to realize micrometer-scale displacement and thin-film thickness sensing around 280 GHz using a single RTD. We (i) present an interferometric signal model tailored to RTD self-mixing, (ii) introduce a simple phase-shift estimator based on this model, and (iii) quantify the robustness of the proposed method through both simulation and experimental results, and (iv) validate the approach experimentally for 5–200  $\mu\text{m}$  displacement and 12.5–50  $\mu\text{m}$  polymer film thickness steps. Compared with conventional THz radar architectures, the proposed approach significantly simplifies the front-end hardware while retaining coherent phase sensitivity, offering a practical and scalable solution for THz-band sensing applications.

## II. METHODOLOGY

### A. THz sensing using RTD self-mixing signal

A resonant-tunneling diode (RTD) is a quantum heterostructure device that exhibits negative differential conductance (NDC) in its current–voltage characteristic owing to resonant tunneling [13]. When the magnitude of the NDC exceeds the loss of an external resonant circuit, self-sustained oscillation can be generated at sub-terahertz or terahertz frequencies [14]. Owing to the strong nonlinearity of the current–voltage (I–V) characteristic, the same device can operate as both a terahertz source and a detector, as illustrated in Fig. 1. Moreover, within a specific bias range the RTD can sustain oscillation while receiving a reflected signal, enabling self-oscillating mixing; this operating regime is commonly referred to as the self-mixing region.

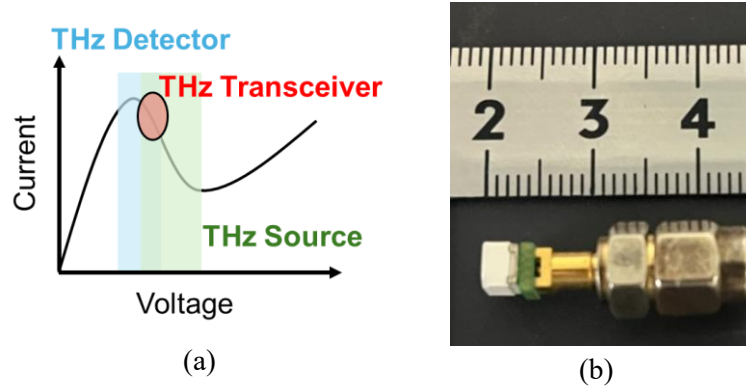


Fig. 1. (a) Conceptual RTD I–V characteristic and bias regions used for oscillation and self-oscillating mixing; (b) photograph of the RTD module used in this work.

For the sensing application, if a portion of the radiated THz signal is reflected by the target and reinjected into the RTD oscillator, giving rise to a low-frequency baseband response commonly referred to as self-mixing. This self-mixing effect enables a single RTD to simultaneously function as a signal source and a nonlinear mixer, thereby supporting highly compact transceiver architectures that consolidate oscillation, mixing, and detection within a single device [17,18]. Notably, the self-mixing effect in an RTD is also referred to as external feedback and is formally analogous to optical self-mixing in semiconductor lasers [16,22].

In both cases, the oscillator dynamics can be modeled as a delay-feedback system closely related to the Lang–Kobayashi framework [24], in which the feedback strength and phase govern waveform distortion and phase sensitivity. According to the Lang–Kobayashi framework,  $\phi_0(f)$  denotes the free-running phase in the absence of self-mixing [22]. When external feedback is present, the phase is modified according to

$$\phi(f) = \phi_0(f) + C \sin(\phi(f) + \psi), \quad (1)$$

and the round-trip propagation phase is:

$$\phi_0(f) = \frac{4\pi f R}{c}. \quad (2)$$

Here,  $c$  is the speed of light,  $f$  is the operating frequency set by the RTD bias voltage,  $R$  is the target range,  $C$  is the feedback coupling factor, and  $\psi$  is a constant phase offset. This indicates that when the emitted field is reflected by a distant target and a portion couples back to the RTD antenna, producing a bias-dependent self-mixing voltage that encodes the round-trip phase. The measurable self-mixing output is typically a periodic function of the feedback-modified phase [22,23]. When the amplitude term is neglected, it can be written as

$$s(\phi_0(f)) = \cos(\phi(f)). \quad (3)$$

The feedback regime is conveniently characterized by  $C$ , which is affected by both the RTD circuit and the reflected power. For weak-to-moderate feedback ( $0 < C < 1$ ), the mapping from  $\phi_0$  to  $\phi$  is generally single-valued and continuous over the phase range of interest, resulting in smooth waveform distortions such as asymmetry and a redistribution of local phase sensitivity, as shown in Fig. 2(a). Although the self-mixing waveform becomes increasingly distorted as  $C$  increases, it remains periodic, indicating that the range information is preserved for accurate distance estimation [18,23], as shown in Fig. 2(b). Moreover, when  $C$  is close to unity, the sharpened waveform provides multiple localized high-contrast features across the sweep, making global waveform alignment more sensitive to small phase translations than a pure sinusoid, where displacement information is concentrated near quadrature points.

Notably, additional attenuation may be required to avoid the strong-feedback regime ( $C > 1$ ), in which the implicit phase equation can admit multiple solutions, leading to branch switching, hysteresis, and abrupt fringe discontinuities that complicate phase demodulation and degrade robust delay estimation. In this work, we restrict attention to the  $0 < C < 1$  regime, consistent with prior reports and our experimental observations using a spatially separated or collimated beam [18], whereas the detailed validation is discussed further in Sec. III(B).

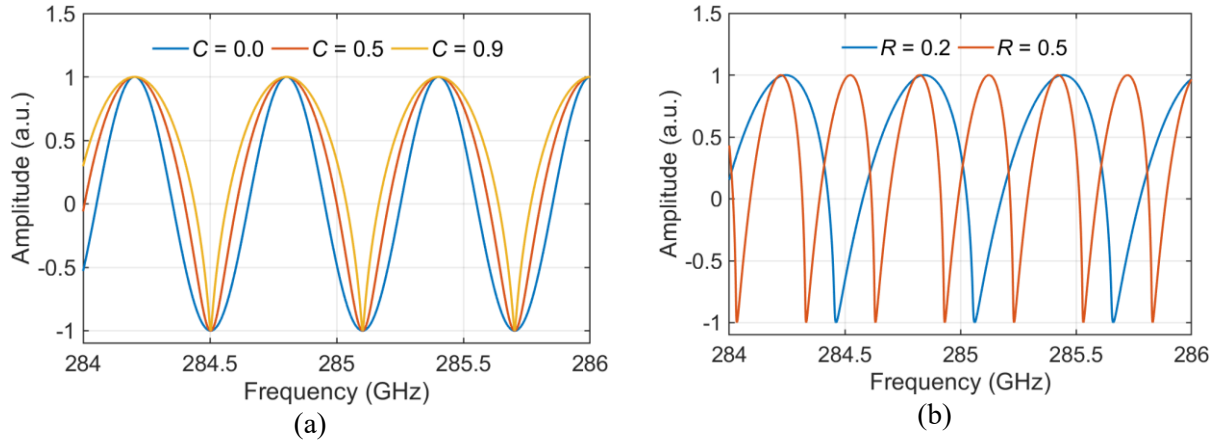


Fig. 2. Simulated RTD self-mixing signals over a 2-GHz bandwidth at 280 GHz: (a) signals for different feedback coupling factors  $C$  (with  $R = 0.2$  m and  $\psi = 0$ ); (b) signals for different target ranges  $R$  (with  $C = 0.9$  and  $\psi = 0.5$ ).

Building on the self-mixing capability demonstrated in Fig. 2(b), a single RTD can be employed to estimate the target distance in a manner analogous to a conventional radar system. Compared with the conventional CW radar architecture illustrated in Fig. 3, the proposed approach integrates oscillation and mixing within a single device. However, radar sensing based on the self-mixing signal differs from a conventional radar system in several key aspects, which are discussed in the next section, and the implementation details of the proposed system are further described in Sec. III(A).

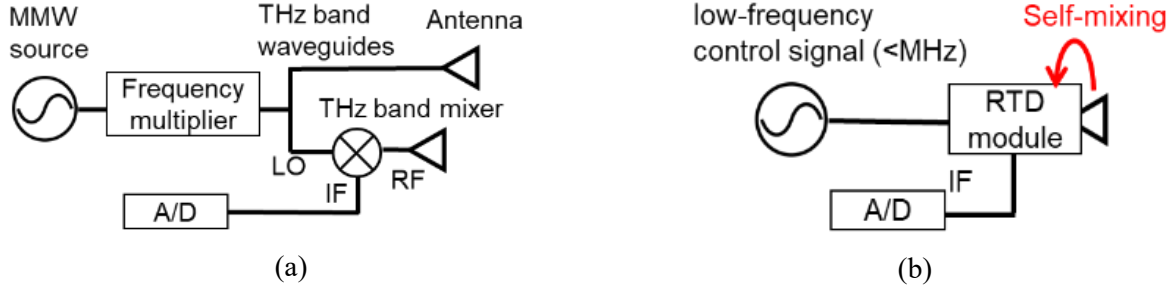


Fig. 3. (a) Conventional radar front-end with separate transmitter and receiver; (b) proposed RTD self-mixing sensing configuration.

## B. Comparison of self-mixing signal and radar beat signal

In a standard CW radar configuration, a single-tone signal at frequency  $f$  is transmitted toward a target at range  $R$  and coherently mixed with a reference derived from the transmitter, as shown in Fig. 3(a) [6]. The detected coherent signal can be written as

$$S_1(f) = A(f)\exp(j(\phi_0(f) + \phi_n)), \quad (4)$$

where the round-trip propagation phase  $\phi_0$  is given in Eq. (2), and  $\phi_n$  denotes phase noise and other frequency-independent phase terms introduced by the measurement chain. In what follows, we omit the amplitude term  $A(f)$  and the constant phase offset  $\phi_n$  for notational convenience.

To extract range information embedded in the phase term, the FMCW radar concept employs a swept carrier frequency. The frequency dependence of  $\phi_0(f)$  encodes the target distance as a low-frequency beat signal, from which the range can be estimated using a Fourier transform. [2, 6]. Notably, taking the real part of the coherent beat signal yields a sinusoidal waveform that is equivalent to the self-mixing signal in the limiting case  $C = 0$ . In other words, as the injected feedback power becomes smaller, the RTD self-mixing signal approaches the conventional radar beat signal.

Compared with conventional radar architectures that rely on a tunable source, low-loss waveguide/quasi-optical front ends, and coherent mixer/LO chains, the proposed RTD self-mixing setup can be significantly more compact and cost-effective, as shown in Fig. 3. However, the feedback coupling factor is target-dependent, which restricts the applicability of the RTD approach to specific scenarios. In addition, operation in the self-mixing regime typically reduces the effective tuning range of the RTD, making it challenging to achieve high-resolution range profiling. In conventional radar, the range resolution is approximately

$$\Delta R = \frac{c}{2B}, \quad (5)$$

where  $B$  is the chirp bandwidth. In contrast to THz-TDS, which employs ultrashort pulses with an effective bandwidth of several terahertz and thereby enables micrometer-scale range resolution for thin-film thickness measurements [3, 9], the maximum tuning bandwidth of an RTD is typically limited to  $\sim 10\%$  of its center frequency. Consequently, in the 280 GHz band, the achievable range resolution is on the order of centimeters.

### C. Simplified interferometric radar technique using self-mixing signal

Given the characteristics of the proposed RTD self-mixing system, it is more appropriate to leverage its high carrier frequency and compact implementation rather than to rely on an extremely large bandwidth. In this context, repeated coherent sweeps establish an interferometric regime in which small phase perturbations can be exploited to estimate micrometer-scale displacements or thickness variations even when the available bandwidth is limited. Such phase-based metrology is widely used in radar remote sensing to measure displacements much smaller than the wavelength [7,8].

Considering a small displacement  $\Delta d$  of the reflector changes the range from  $R$  to  $R + \Delta d$ , the radar beat signal after displacement can be written as

$$S_2(f) = A(f)\exp\left(-j\frac{4\pi}{c}f(R + \Delta d)\right) = S_1(f)\exp\left(-j\frac{4\pi}{c}f\Delta d\right). \quad (6)$$

For a conventional radar configuration, the micro-displacement introduces an additional linear phase term versus frequency and  $\Delta d$  can be estimated using cross-correlation

$$\Delta\phi(f) \triangleq \angle\{S_1^*(f)S_2(f)\} = \frac{4\pi f}{c}\Delta d. \quad (7)$$

However, for the RTD self-mixing signal it is difficult to obtain a reliable complex representation. Moreover, the waveform is distorted in a feedback-dependent manner, which complicates the direct application of conventional interferometric radar methods. In this case, it is convenient to adopt a more general waveform-shift viewpoint under the narrowband assumption [8,25], which assumes that over a swept bandwidth  $B$ , the differential phase variation  $\Delta\phi_{\text{across}}$  induced by  $\Delta d$  is bounded by

$$\Delta\phi_{\text{across}} = \frac{2\pi B}{c}\Delta d \ll 1. \quad (8)$$

For micrometer-scale displacement sensing around 300 GHz, this requirement is well satisfied: with a bandwidth of 5 GHz,  $\Delta\phi_{\text{across}}$  is only 0.002 rad for  $\Delta d = 10 \mu\text{m}$ . Thus, the phase factor  $\Delta\phi(f)$  is approximately constant across the bandwidth; we evaluate this phase difference at an effective carrier  $f_c$ , treating it as a frequency-independent constant so that the  $\Delta d$  can be quantified with

$$\Delta\phi_c \triangleq \Delta\phi(f_c) = \frac{4\pi f_c}{c}\Delta d. \quad (9)$$

The constant small phase offset provides the link to the “shift” interpretation of beat/self-mixing signal: if the measured sweep is a periodic readout  $s[k] = g(\phi_k)$  of a monotonically swept phase variable  $\phi_k$  (with  $k$  denoting the sweep index or frequency sample), then the second sweep is well approximated by

$$S_2[k] \approx g(\phi_k + \Delta\phi_c) \approx S_1[k + \Delta k], \Delta k \approx \frac{\Delta\phi_c}{d\phi/dk}, \quad (10)$$

This shift-based viewpoint can also be applied to self-mixing signals under two conditions. First, the phase mapping  $\phi(\phi_0)$  must remain locally smooth and single-valued. This condition is satisfied when the RTD is not operated in the strong-feedback regime ( $C > 1$ ), where hysteresis and abrupt fringe discontinuities can occur, as discussed in Sec. II(A). Second, the narrowband assumption must hold. Under these conditions,

a small constant increment in the free-running phase  $\phi_0$  propagates to a small, approximately constant increment in  $\phi$ , preserving the local shift model in Eq. (10) even when waveform distortion is pronounced. As shown in Fig. 4, the simulated self-mixing signal with  $C = 0.7$  appears as an approximately shifted waveform for displacements up to 200  $\mu\text{m}$ , assuming a 280 GHz center frequency and a 2 GHz sweep bandwidth.

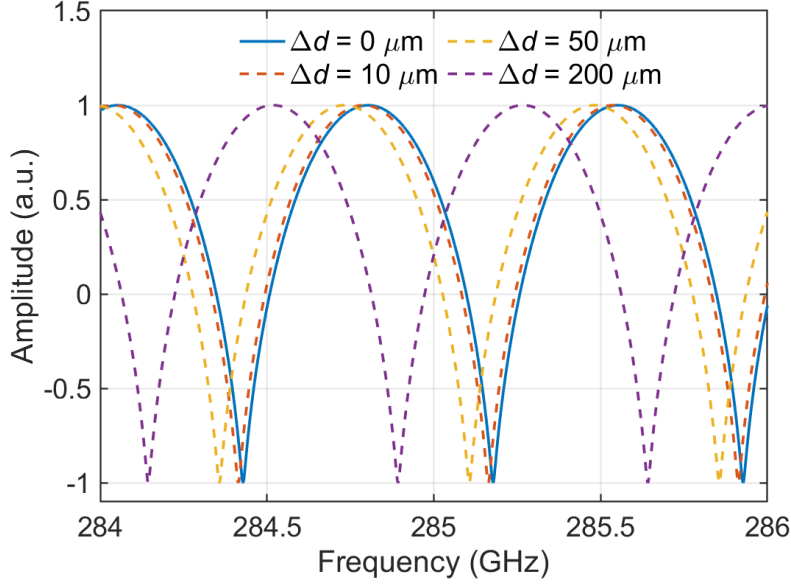


Fig. 4. Simulated self-mixing waveforms for different target displacements ( $\Delta d = 0, 10, 50,$  and  $200 \mu\text{m}$ ) over a 2-GHz sweep, illustrating the approximate waveform shift used for displacement estimation (with  $C = 0.9$  and  $\psi = 0$ ).

#### D. Phase-delay estimation for interferometric radar configuration

To robustly estimate small phase shifts between successive interferometric sweeps in the presence of waveform distortion and baseline drift, we adopt a bounded normalized cross-correlation (NCC) approach [26,27]. After removing the mean from both signals, we computed the NCC within a prescribed lag window and selected the integer-sample delay as the lag that maximized the correlation. For each candidate integer shift  $k$  within a predefined bound  $[k_{\min}, k_{\max}]$ , fixed-length overlapping segments of  $S_1[n]$  and  $S_2[n - k]$  are extracted. The mean value of each segment is removed prior to correlation, and the normalized cross-correlation coefficient is computed as

$$\rho(k) = \frac{\sum_{n \in \Omega_k} (S_1[n] - \bar{S}_{1k})(S_2[n-k] - \bar{S}_{2k})}{\sqrt{\sum_{n \in \Omega_k} (S_1[n] - \bar{S}_{1k})^2 \sum_{n \in \Omega_k} (S_2[n-k] - \bar{S}_{2k})^2}}, \quad (11)$$

where  $\Omega_k$  denotes the fixed-length overlap window and  $\bar{S}_{1k}, \bar{S}_{2k}$  are the local means. The delay estimate  $\hat{k}$  is obtained by maximizing  $\rho(k)$  within the bounded interval. To achieve sub-sample accuracy, we refined the peak location by three-point parabolic interpolation around the discrete maximum (using the peak and its two neighbors), a widely used interpolation strategy for cross-correlation-based delay estimation [27]. Finally, the estimated small phase shift can be further converted into the corresponding physical displacement  $\Delta d$  with

$$\Delta d \approx \frac{kR\Delta f}{f_c}, \quad (12)$$

where  $k$  is the estimated sample delay,  $R$  is the distance to the observed target,  $f_c$  is the center frequency and  $\Delta f$  is the frequency step. The bounded NCC estimator leverages the time shift between the two signals by correlating the entire waveform, thereby improving robustness through global information aggregation. To avoid the multi-peak ambiguity inherent in periodic self-mixing signals, the delay search is restricted to a bounded lag window smaller than half of the self-mixing period, thereby ensuring a unique correlation peak. This constraint, however, limits the unambiguous measurable displacement to within half a wavelength.

Based on the self-mixing model and the bounded NCC estimator, the numerical simulation results are summarized in Table I. For each condition, 500 repeated trials were performed with different displacement shifts, where  $\sigma$  denotes the standard deviation of additive white Gaussian noise relative to the normalized signal amplitude. The root-mean-square error (RMSE) of the estimated shift was then recorded. The results suggest that the displacement estimation can achieve a high resolution of approximately 1  $\mu\text{m}$ . Also, across a wide range of noise levels, the self-mixing cases ( $C = 0.6$  and  $C = 0.9$ ) achieve comparable or lower RMSE than the ideal sinusoid ( $C = 0$ ). This supports the intuition that self-mixing redistributes phase sensitivity across multiple high-slope intervals, so more samples carry useful displacement information.

Table I. RMSE of the estimated displacement  $\Delta d$  under different additive noise levels ( $\sigma$ ) and feedback factors  $C$ . Values are given in  $\mu\text{m}$ .

Noise $\sigma$	$\Delta d = 10 \mu\text{m}$			$\Delta d = 50 \mu\text{m}$			$\Delta d = 200 \mu\text{m}$		
	$C = 0$	$C = 0.5$	$C = 0.9$	$C = 0$	$C = 0.5$	$C = 0.9$	$C = 0$	$C = 0.5$	$C = 0.9$
0.01	0.089	0.098	0.074	0.163	0.182	0.132	0.083	0.099	0.068
0.05	0.590	0.621	0.491	0.614	0.675	0.496	0.583	0.622	0.534
0.1	1.191	1.001	0.913	1.104	1.103	0.993	1.616	1.323	1.000

### III. SYSTEM IMPLEMENTATION AND EXPERIMENT

#### A. Integrated THz radar module using a single RTD

In this work, a packaged RTD module provided by ROHM Co., Ltd. is used to demonstrate sensing in the 280-GHz band. The RTD chip has an area of approximately 0.02  $\text{mm}^2$  and is mounted behind a dielectric antenna, as shown in Fig. 1(b) [15]. The I–V characteristic is measured using a DC source, and the corresponding oscillation frequency is characterized with a spectrum analyzer, as shown in Fig. 5(a). Notably, to better satisfy the narrowband assumption for detecting smaller displacements, we choose a bias range of 0.36–0.365 V to ensure good frequency linearity, which provides an effective tuning span of approximately 2 GHz and satisfies the narrowband assumption, as shown in Fig. 5(b). The output power of a single RTD device is approximately 20  $\mu\text{W}$ .

The measurement configuration is summarized in Fig. 6(a). To acquire the RTD self-mixing signal, a low-frequency sawtooth bias waveform is applied to periodically sweep the device through the self-mixing region, thereby tuning the oscillation frequency over the selected range. The bias voltage  $V_{\text{bias}}$  is generated by the digital-to-analog converter of a commercial field programmable gate array (FPGA) and connected to a T-connector (Port 1).

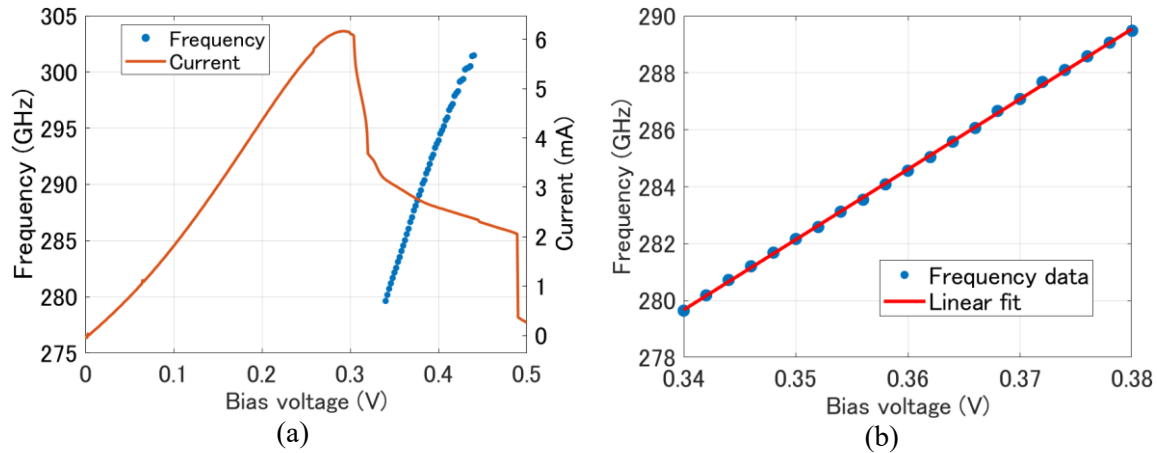


Fig. 5. (a) The corresponding oscillation frequency (left axis) of the packaged RTD module, and the RTD current–voltage ( $I$ – $V$ ) characteristic (right axis) of the packaged RTD module, with the effect of the shunt resistance compensated. (b) linear frequency tuning in the selected bias range (0.34–0.38 V) used for frequency sweeps.

During each sweep, the RTD connected to Port 2 of the T-connector operates in the self-mixing regime. The reinjected field induces a small self-mixing perturbation  $V_{\text{RTD}}$ , which is superimposed on the applied bias voltage  $V_{\text{bias}}$ . Since the self-mixing signal  $V_{\text{RTD}}$  is much smaller than the applied bias, it is not directly observable at the RTD terminals. To extract the self-mixing signal, we employ a differential amplifier at Port3 of the T-connector to suppress the large bias component by injecting a synchronized bias voltage  $V'_{\text{bias}}$ . Finally, the amplified self-mixing signal  $GV_{\text{RTD}}$  is acquired using the analog-to-digital converter (ADC) of the same FPGA or an oscilloscope.

Because both the bias signal and the self-mixing signal reside in the baseband (typically kHz–MHz), the required electronics can be implemented with a standard arbitrary waveform generator and a moderate-speed digitizer. As shown in Fig. 6(b), an integrated RTD sensing system was developed using a commercial USB instrument together with a compact control circuit to generate the sawtooth bias and digitize the RTD self-mixing signal. This is in contrast to many THz coherent ranging architectures that require high-speed intermediate-frequency processing or an external coherent local oscillator.

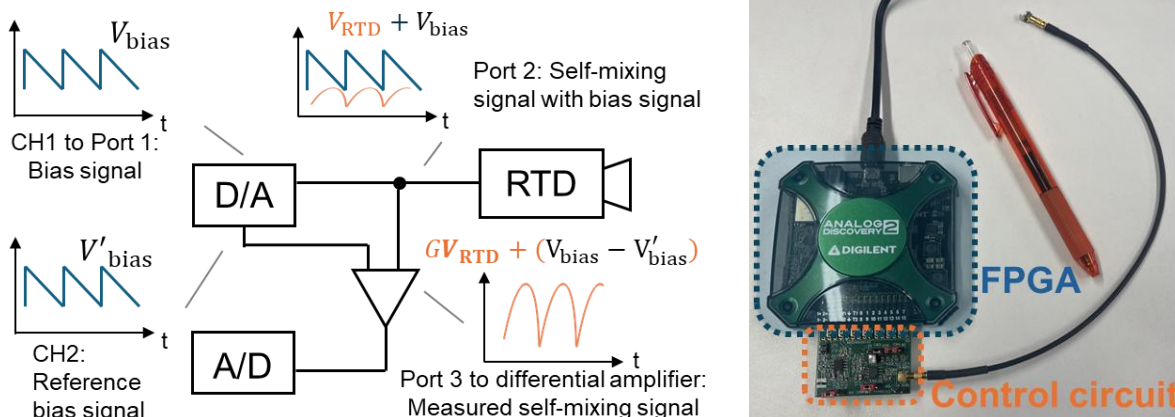


Fig. 6. (a) The configuration of the proposed RTD sensing system, (b) Photograph of the integrated prototype of the proposed system.

## B. Evaluation of the RTD sensing system

To evaluate the performance of the proposed system, self-mixing signals from a metallic reflector were measured at different distances using the experimental arrangement shown in Fig. 7(a). Figure 7(b) shows the sampled self-mixing signals for a metallic reflector placed at distances of 25, 40, and 70 cm, demonstrating the ranging capability and potential for three-dimensional imaging [18]. Owing to the high sensitivity of self-mixing signal [14,17], the radar signal remains detectable up to 70 cm even with a relatively low output power of approximately  $20 \mu\text{W}$ .

Notably, although the THz beam was collimated at the source, beam divergence over longer propagation distances reduced the reflected power incident on the RTD. By fitting the measured self-mixing signal in Fig. 8 to the self-mixing model with a constant phase offset  $\psi = 0.7$  and noise  $\sigma = 0.05$ , the effective feedback factor  $C$  is estimated to be approximately 0.7 under the collimated condition. Notably, this value is expected to decrease when the reflector size is reduced or when the alignment is imperfect, since the returned power coupled back into the RTD becomes weaker.

The ADC captured the raw waveform directly; a simple moving average was applied to reduce system noise. For a metallic reflector placed 25 cm from the sensor, the relationship between modulation speed and the required averaging factor is summarized in Fig. 9. The standard deviation (STD) over 500 repeated measurements was computed from the phase offset estimated for each sweep using the method described in Sec. II(D). The mean value and corresponding STD quantify the stability of the self-mixing signal. As the modulation speed increases, a longer moving-average window is required to achieve comparable noise suppression. This may be related to reduced injection-locking stability when the transmitted and reflected signals change rapidly, leading to less effective phase-noise suppression [28]. In the following experiments, a modulation speed of 10 kHz was selected, and 1024 sweeps were averaged, yielding an acquisition time of approximately 10 ms. Each self-mixing sweep spanning 284–286 GHz was sampled with 1000 points, resulting in a frequency step  $\Delta f$  of approximately 2 MHz.

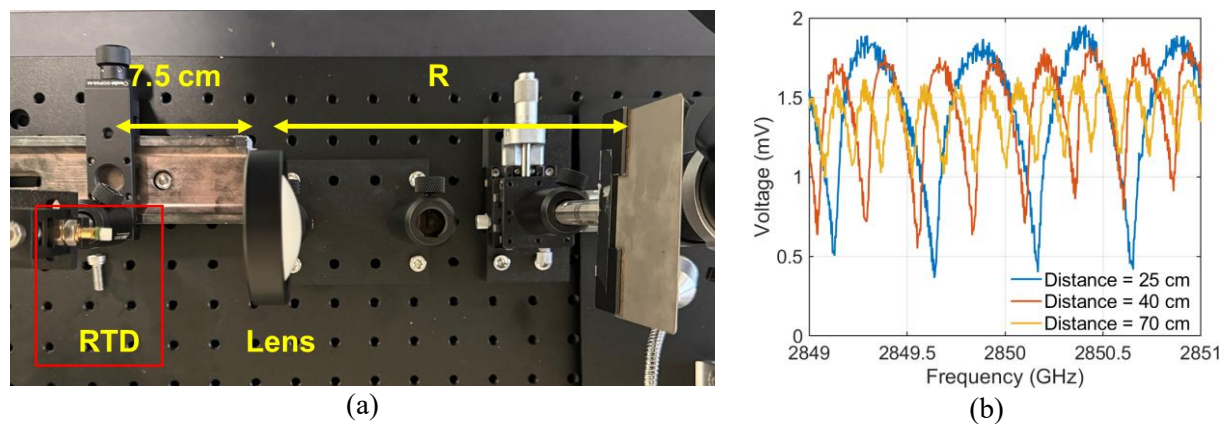


Fig. 7. (a) photograph of the experimental arrangement for ranging, and displacement measurements; (b) the obtained self-mixing signal of metallic reflector at different distances.

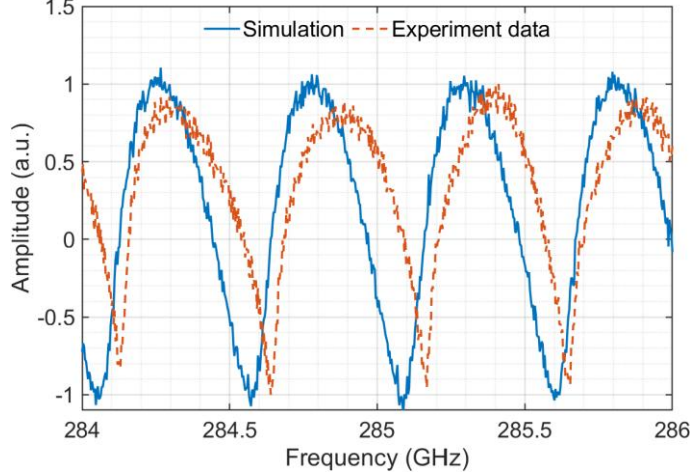


Fig.8 Simulated and experimentally measured self-mixing signal for a metallic reflector at 25 cm (with  $C = 0.7$ ,  $\psi = 0.7$  and noise  $\sigma = 0.05$ ).

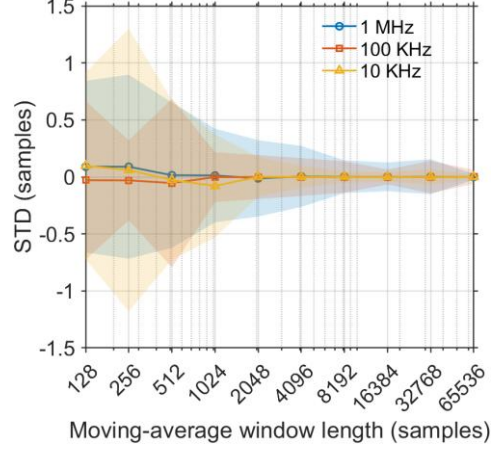


Fig. 9 Relationship between sweep modulation speed and the required moving-average window length.

Finally, since the self-mixing signal is recorded versus bias voltage rather than versus oscillation frequency, the relation between the bias voltage and the oscillation frequency should be characterized, as shown in Fig. 5(b). However, measuring the RTD oscillation frequency requires a high-end spectrum analyzer, and the measured frequency can also vary with reflected power. In practice, a calibration can be obtained by measuring a reference target at a few known displacements and calibrating the system for a specific working distance using Eq. (10), which directly maps the bias-voltage shift to the displacement  $\Delta d$ . With this mapping, the displacement can be calculated directly using Eq. (12).

### C. Displacement and thin film thickness measurement

To demonstrate small-displacement sensing, the same experimental configuration as in Fig. 7(a) was used. Figure 10 summarizes the displacement sensing results for commanded translation steps from 5 to 200  $\mu\text{m}$ . A metallic reflector was placed at a distance of  $\sim 25$  cm, and controlled displacements were applied using a high-precision opto-mechanical translation stage. For each commanded displacement, 50 repeated measurements were performed to evaluate repeatability. The estimated displacement agrees well with the commanded displacement, whereas the measurement spread increases for step sizes ranging from 10  $\mu\text{m}$  to 200  $\mu\text{m}$ , as shown in Fig. 10(a). A finer step size of 5  $\mu\text{m}$  was also evaluated up to 50  $\mu\text{m}$ , as shown in Fig. 10(b). The increased spread at smaller steps is consistent with the reduced phase excursion and the greater susceptibility to residual drift. The distributions of the measured displacements relative to the ground truth are presented as box plots. These results suggest that a practical displacement resolution on the order of  $\sim 10$   $\mu\text{m}$  is achievable with the proposed system under the current experimental conditions. Although Fig. 9 indicates a relatively low noise level in the self-mixing signal, the reduced accuracy at small steps may be attributed to slow drift of the self-mixing waveform over time and temperature variations. In addition, because the small displacements were manually adjusted, the results may also include uncertainties associated with the translation stage and manual operation.

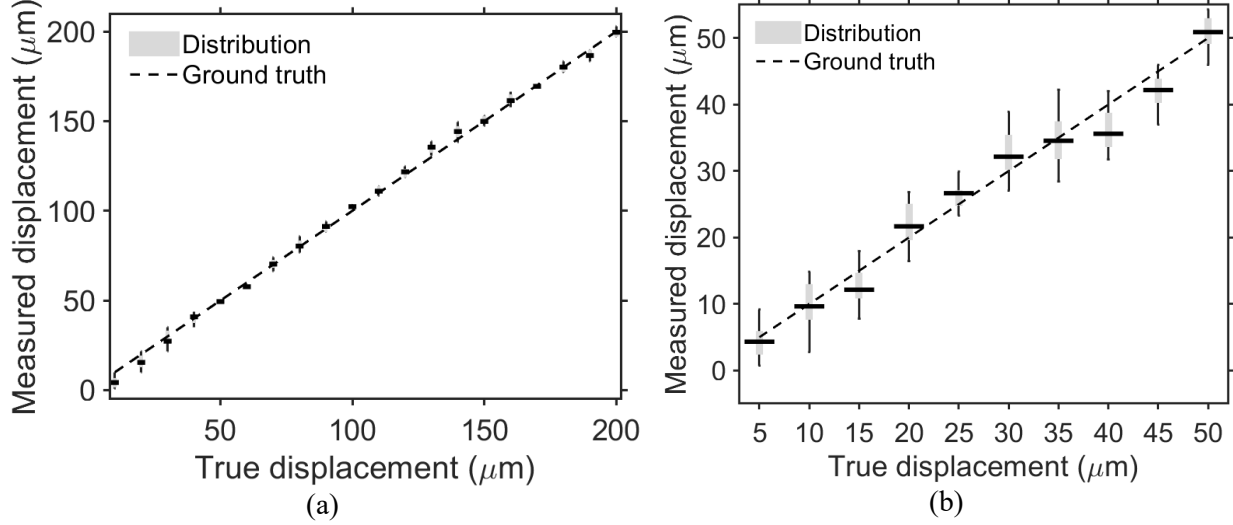


Fig. 10 Distribution of measured displacements at different true displacement values; (a) measurement results up to 200  $\mu\text{m}$ , (b) measurement results up to 50  $\mu\text{m}$ . Each box represents 50 repeated measurements, showing the median (central line), interquartile range (box), and whiskers ( $1.5 \times \text{IQR}$ ). The dashed line indicates the ground truth.

Table II. Statistical Summary of Measured Displacements ( $N = 50$  per sample)

Ground truth ( $\mu\text{m}$ )	Mean ( $\mu\text{m}$ )	Std. Dev. ( $\mu\text{m}$ )	Bias ( $\mu\text{m}$ )	RMSE ( $\mu\text{m}$ )
12.5	14.039	3.249	2.039	3.808
25.0	27.807	1.650	2.807	3.248
50.0	47.898	2.274	-2.102	3.080

For thin-film thickness sensing, we consider a dielectric film with refractive index  $n$  placed between the RTD and a metallic reference reflector, as shown in Fig. 11(a). Notably, an extra lens was included to obtain a better spatial resolution. Compared with the bare reflector, inserting a film of thickness change  $\Delta z$  replaces an air path of  $\Delta z$  with an optical path  $n\Delta z$ , resulting in an additional round-trip optical path difference of  $2(n - 1)\Delta z$ . Accordingly, the film-induced change can be treated as an equivalent air-path displacement  $(n - 1)\Delta z$ , leading to

$$\Delta z \approx \frac{kR\Delta f}{f_c(n - 1)}. \quad (13)$$

Table II. summarizes the thickness estimation results for polymer films with nominal thicknesses of 12.5, 25, and 50  $\mu\text{m}$ . Each sample was measured repeatedly to evaluate the measurement statistics. An RMSE of approximately 3  $\mu\text{m}$  is obtained across the three samples. As the target is translated laterally, the estimated thickness shows step-like transitions corresponding to the inserted film thickness. Notably, the refractive index of the sample was estimated to be approximately 1.7, which is in good agreement with the manufacturer-specified value. Since the equivalent air-path displacement associated with a 12.5  $\mu\text{m}$  film is on the order of  $\sim 8$   $\mu\text{m}$ , this thickness is close to the practical detection limit of the proposed approach under the current experimental conditions.

For a more practical demonstration, the films were secured in a 3D-printed holder mounted on a translation stage for thickness-difference measurements. In this case, each lateral position was measured

once using a focused THz beam, yielding an effective spatial resolution of approximately 2 mm to separate adjacent samples. Despite uncertainties in the effective refractive index and film positioning, the results demonstrate that micrometer-scale thickness steps can be resolved with the proposed system, as shown in Fig. 11(b).

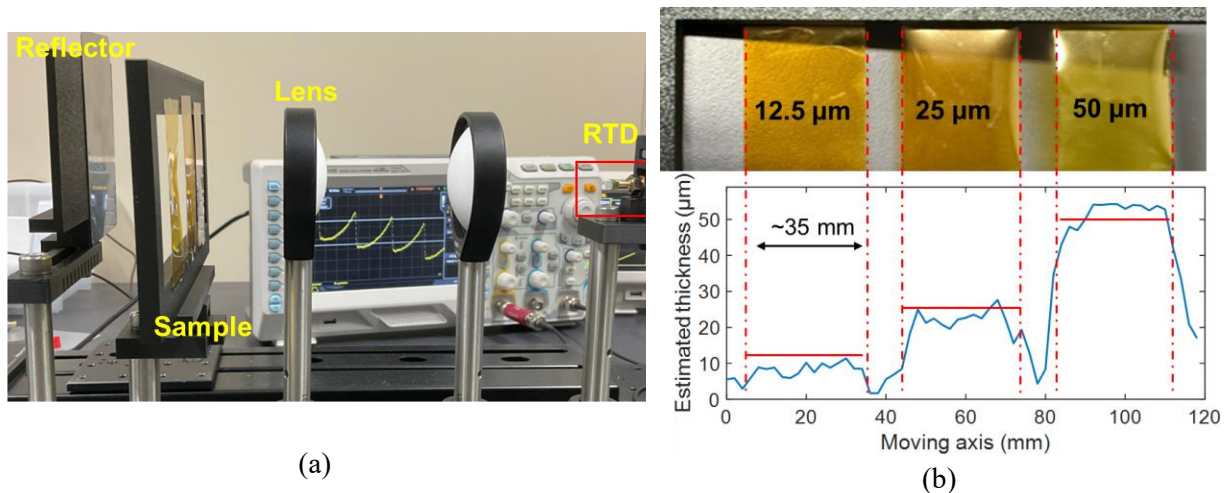


Fig. 11 (a) Photograph of the experimental setup; (b) estimated film thickness along a lateral scan over regions covered by 12.5  $\mu\text{m}$ , 25  $\mu\text{m}$ , and 50  $\mu\text{m}$  polymer films.

#### IV. DISCUSSION

The results highlight several practical features of RTD self-mixing metrology. First, the architecture is inherently compact because coherent mixing occurs directly inside the RTD, and only baseband electronics are required for bias control and signal readout. Second, self-mixing nonlinearity can be beneficial for small-shift estimation by providing multiple high-slope regions within a single interference period. However, strong external feedback can destabilize the oscillator and may necessitate the use of an external attenuator. In addition, it is important to clearly define the operating scenario to avoid large variations in the feedback factor  $C$ .

To fully exploit the advantages of the RTD sensor, an interferometric radar approach is introduced to leverage its high center frequency, making it well suited for monitoring small vibrations and detecting thickness variations in thin films. In these scenarios, the phase information at the center frequency becomes critical for accurate detection, enabling the possibility of resolving micrometer-scale displacements with the proposed approach. Moreover, since the displacement-to-phase conversion scales with frequency, operation at higher RTD oscillation frequencies (e.g., in the 2 THz band [14]) could, in principle, further improve the displacement sensitivity toward the nanometer scale, provided that the signal-to-noise ratio and phase stability are sufficient. On the other hand, small displacements or thin dielectric layers only weakly perturb the feedback condition, so the feedback factor  $C$  does not vary abruptly, allowing the phase-shift approximation described in Sec. II(B) to remain valid. However, it should be noted that, owing to the unique operating mechanism of RTD self-mixing, it remains challenging to quantitatively characterize the phase noise and ultimate sensitivity of the proposed technique. In addition, phase noise, which may be caused by the noise of the DAC board, the injection power into the RTD, and temperature variations, limits

the minimum achievable estimation accuracy and warrants further investigation from a device-physics perspective.

In the present thickness demonstration, a single effective refractive index is used to convert frequency shifts into thickness variations. For quantitative metrology of unknown materials, the refractive index may be obtained through independent characterization methods (e.g., THz-TDS) or by exploiting multi-frequency information across the frequency sweep. Although it is mathematically possible to invert thickness changes in multilayer structures, the resulting computational complexity limits the practicality of such approaches [10]. Consequently, the proposed method is more suitable for detecting thickness variations or localized defects in layered samples.

Finally, the proposed system operates entirely with low-frequency circuitry in the sub-MHz range, which facilitates straightforward extension to a monostatic array configuration using only microwave components. When combined with high-speed switching components, this architecture enables the realization of a THz-band imaging system in which each RTD simultaneously functions as a transmitter and a detector. Compared with THz array systems implemented using CMOS technology, the proposed configuration offers significant reductions in system size and power consumption.

## V. CONCLUSION

We presented a compact THz radar sensor based on a single resonant-tunneling diode operating near 280 GHz. By sweeping the RTD bias to generate a frequency sweep and measuring the resulting self-mixing waveform, micrometer-scale displacement and thin-film thickness changes can be inferred from small phase shifts using an interferometric radar approach. The proposed technique was validated using both numerical simulations and experimental measurements. The system demonstrated displacement sensing over 5–200  $\mu\text{m}$  and resolved polymer film thickness steps down to 12.5  $\mu\text{m}$ , highlighting the potential of single-device RTD self-mixing for compact THz metrology.

## Acknowledgement

The authors gratefully acknowledge ROHM Co., Ltd. for financial support and for providing the RTD devices. This work was also partially supported by the BOOST, JST (JPMJBY25A1), the CREST, JST (JPMJCR21C4) and the Multidisciplinary Research Laboratory System of the Graduate School of Engineering Science, Osaka University.

## REFERENCES

- [1] D. M. Mittleman, “Twenty years of terahertz imaging,” *Opt. Express*, vol. 26, no. 8, pp. 9417–9431, 2018.
- [2] L. Yi, Y. Nishida, T. Sagisaka, R. Kaname, R. Mizuno, M. Fujita, and T. Nagatsuma, “Towards practical terahertz imaging systems with compact continuous-wave transceivers,” *J. Lightwave Technol.*, vol. 39, no. 24, pp. 7850–7861, 2021.
- [3] M. Koch, D. M. Mittleman, J. Ornik and E. Castro-Camus, “Terahertz time-domain spectroscopy,” *Nat. Rev. Methods Primers*, vol. 3, Art. no. 49, 2023.

- [4] P. U. Jepsen, D. G. Cooke, and M. Koch, "Terahertz spectroscopy and imaging—Modern techniques and applications," *Laser Photon. Rev.*, vol. 5, no. 1, pp. 124–166, 2011.
- [5] L. Yi, Y. Li and T. Nagatsuma, "Photonic Radar for 3D Imaging: From Millimeter to Terahertz Waves," in *IEEE Journal of Selected Topics in Quantum Electronics*, vol. 29, no. 5: Terahertz Photonics, pp. 1-14
- [6] M. A. Richards, J. A. Scheer, and W. A. Holm, *Principles of Modern Radar: Basic Principles*. Raleigh, NC, USA: SciTech Publishing, 2014.
- [7] A. Moreira, P. Prats-Iraola, M. Younis, G. Krieger, I. Hajnsek, and K. P. Papathanassiou, "A tutorial on synthetic aperture radar," *IEEE Geosci. Remote Sens. Mag.*, vol. 1, no. 1, pp. 6–43, Mar. 2013.
- [8] P. A. Rosen, S. Hensley, I. R. Joughin, F. K. Li, S. N. Madsen, E. Rodriguez, and R. M. Goldstein, "Synthetic aperture radar interferometry," *Proc. IEEE*, vol. 88, no. 3, pp. 333–382, 2000.
- [9] L. Liebermeister, S. Nellen, R. B. Kohlhaas, *et al.*, "Optoelectronic frequency-modulated continuous-wave terahertz spectroscopy with 4 THz bandwidth," *Nature Communications*, vol. 12, Art. no. 1071, 2021.
- [10] N. S. Schreiner, D. J. Bock, M. Hoffmann, V. Krozer, and N. Pohl, "Multilayer thickness measurements below the Rayleigh limit using FMCW millimeter and terahertz waves," *Sensors*, vol. 19, no. 18, Art. no. 3910, 2019.
- [11] K. O. Kenneth, W. Choi, and R. Han, "Perspective on active submillimeter electromagnetic wave imaging using CMOS integrated circuit technologies," *J. Appl. Phys.*, vol. 133, no. 15, Art. no. 150903, Apr. 2023.
- [12] T. Ziegler-Bellenberg, D. Funke, C. Bredendiek, S. Hansen, J. Wessel, and N. Pohl, "A high-resolution 300-GHz FMCW-radar sensor using a dual-function SiGe transceiver MMIC," *Int. J. Microw. Wireless Technol.*, vol. 17, no. 9, pp. 1–13, Aug. 2025.
- [13] S. Suzuki, "Fundamentals and recent advances of terahertz resonant tunneling diodes," *Appl. Sci.*, vol. 12, no. 7, Art. no. 3822, 2022.
- [14] M. Asada and S. Suzuki, "Room-temperature oscillation of resonant tunneling diodes close to 2 THz and their functions for various applications," *J. Infrared Millim. Terahz. Waves*, vol. 37, no. 12, pp. 1185–1198, 2016.
- [15] K. Tsuruda *et al.*, "Development of practical terahertz packages for resonant tunneling diode oscillators and detectors," in *Proc. IEEE Int. Symp. Radio-Frequency Integration Technology (RFIT)*, Hiroshima, Japan, 2020, pp. 193–195.
- [16] M. Asada and S. Suzuki, "Theoretical analysis of external feedback effect on oscillation characteristics of resonant-tunneling-diode terahertz oscillators," *Jpn. J. Appl. Phys.*, vol. 54, no. 7, Art. no. 070309, 2015.
- [17] Y. Nishida, N. Nishigami, S. Diebold, J. Kim, and M. Fujita, "Terahertz coherent receiver using a single resonant tunnelling diode," *Sci. Rep.*, vol. 9, Art. no. 18125, 2019.

- [18] L. Yi, Y. Inose, N. Ngo, S. Wang, Y. Nishida, and M. Fujita, "Resonant tunneling diode transceiver for integrated terahertz-band 3D image sensors," in Proc. 49th Int. Conf. Infrared, Millimeter, and Terahertz Waves (IRMMW-THz), Perth, Australia, 2024.
- [19] S. Suzuki, A. Dobroiu, and M. Asada, "Resonant-tunneling-diode terahertz oscillators and its radar applications," *The Review of Laser Engineering*, vol. 50, no. 4, pp. 183–187, 2022.
- [20] A. Dobroiu, Y. Shirakawa, S. Suzuki, M. Asada, and H. Ito, "Subcarrier frequency-modulated continuous-wave radar in the terahertz range based on a resonant-tunneling-diode oscillator," *Sensors*, vol. 20, no. 23, Art. no. 6848, 2020.
- [21] H. Konno, A. Dobroiu, S. Suzuki, M. Asada, and H. Ito, "Discrete Fourier transform radar in the terahertz-wave range based on a resonant-tunneling-diode oscillator," *Sensors*, vol. 21, no. 13, Art. no. 4367, 2021.
- [22] S. Donati, "Developing self-mixing interferometry for instrumentation and measurements," *Laser Photon. Rev.*, vol. 6, no. 3, pp. 393–417, 2012.
- [23] G. Giuliani, M. Norgia, S. Donati, and T. Bosch, "Laser diode self-mixing technique for sensing applications," *J. Opt. A: Pure Appl. Opt.*, vol. 4, no. 6, pp. S283–S294, 2002.
- [24] R. Lang and K. Kobayashi, "External optical feedback effects on semiconductor injection laser properties," *IEEE J. Quantum Electron.*, vol. 16, no. 3, pp. 347–355, 1980.
- [25] A. Amar and A. J. Weiss, "Localization of narrowband radio emitters based on Doppler frequency shifts," *IEEE Transactions on Signal Processing*, vol. 56, no. 11, pp. 5500–5508, Nov. 2008.
- [26] C. H. Knapp and G. C. Carter, "The generalized correlation method for estimation of time delay," *IEEE Trans. Acoust., Speech, Signal Process.*, vol. 24, no. 4, pp. 320–327, 1976.
- [27] L. Svilainis, K. Lukoseviciute, V. Dumbrava, and A. Chaziachmetovas, "Subsample interpolation bias error in time of flight estimation by direct correlation in digital domain," *Measurement*, vol. 46, no. 10, pp. 3950–3958, Dec. 2013.
- [28] B. Razavi, "A study of injection locking and pulling in oscillators," *IEEE J. Solid-State Circuits*, vol. 39, no. 9, pp. 1415–1424, Sep. 2004.